Energy Materials

Article

Organic-inorganic hybrid quasi-2D perovskites incorporated with fluorinated additives for efficient and stable four-terminal tandem solar cells

Yuren Xia[1,#], Mengfei Zhu[1,#], Lina Qin[1,#], Cheng Zhao[1], Daocheng Hong[1], Yuxi Tian[1], Wensheng Yan[2,3,*], Zhong Jin[1,4,5,*]

[1]State Key Laboratory of Coordination Chemistry, MOE Key Laboratory of Mesoscopic Chemistry, MOE Key Laboratory of High Performance Polymer Materials and Technology, Jiangsu Key Laboratory of Advanced Organic Materials, School of Chemistry and Chemical Engineering, Nanjing University, Nanjing 210023, Jiangsu China.
[2]Institute of Carbon Neutrality and New Energy, School of Electronics and Information, Hangzhou Dianzi University, Hangzhou 310018, Zhejiang, China.
[3]Institute of Microstructure Technology (IMT), Institute of Nanotechnology (INT), Karlsruhe Institute of Technology (KIT), Hermann-von-Helmholtz-Platz 1, Eggenstein-Leopoldshafen 76344, Germany.
[4]Nanjing Tieming Energy Technology Co. Ltd., Nanjing 210093, Jiangsu, China.
[5]Suzhou Tierui New Energy Technology Co. Ltd., Suzhou 215228, Jiangsu, China.
[#]Authors contributed equally.

[*]**Correspondence to:** Prof. Wensheng Yan, Institute of Carbon Neutrality and New Energy, School of Electronics and Information, Hangzhou Dianzi University, No. 1158, Baiyang Street, Hangzhou 310018, Zhejiang, China. E-mail: yws118@163.com;
Prof. Zhong Jin, State Key Laboratory of Coordination Chemistry, MOE Key Laboratory of Mesoscopic Chemistry, MOE Key Laboratory of High Performance Polymer Materials and Technology, Jiangsu Key Laboratory of Advanced Organic Materials, School of Chemistry and Chemical Engineering, Nanjing University, No. 163, Xianlin Road, Nanjing 210023, Jiangsu, China. E-mail: zhongjin@nju.edu.cn

Abstract

Quasi-two-dimensional (2D) lead halide perovskites have emerged as promising candidates for improving the environmental stability of perovskite solar cells (PSCs). Herein, we report the preparation of a new quasi-2D perovskite by introducing a fluorine-containing additive [3-(trifluoromethyl)benzylammonium iodide (3-TFMBAI)] into $Cs_{0.17}FA_{0.83}Pb(I_{0.83}Br_{0.17})_3$. The moderate doping of 3-TFMBAI effectively induces the formation of the Ruddlesden-Popper perovskite phase, which can passivate the trap states and restrain the ionic motion in the perovskite lattice. The constructed 3-(trifluoromethyl)benzylamine molecular planes with strong hydrophobicity favorably suppress the decomposition and collapse of the perovskite phase against humidity. Moreover, the

introduction of Cs^+ and Br^- ions tune the bandgap and improve the absorption, crystallinity and thermal stability of the perovskite films. As a result, a champion photoelectric conversion efficiency (*PCE*) of 20.89% is achieved, along with an improved open-circuit voltage reaching 1.22 V. The quasi-2D PSCs without encapsulation maintain 90.7% of the initial *PCE* after 1000 h under continuous heating at 60 °C and simultaneous exposure to humid air with a relative humidity of 60%. Four-terminal tandem solar cells are fabricated by combining top semi-transparent quasi-2D PSCs with bottom monocrystalline silicon solar cells, achieving an overall *PCE* of 23.53% and favorable performance stability.

INTRODUCTION

In the past decade, organic-inorganic hybrid metal perovskites have attracted enormous interest in photovoltaics due to their exceptional photophysical properties, such as large light absorption coefficients, tunable bandgaps, long radiative lifetimes and excellent defect tolerance[1-4]. The photoelectric conversion efficiency (*PCE*) of perovskite solar cells (PSCs) has rapidly increased from 3.8% to 25.8%[5,6], making these novel materials competitive candidates for solar power harvesting. However, PSCs are sensitive to heat, humidity and ultraviolet light, which seriously limits their industrial development and commercialization[7]. In order to improve the tolerance of PSCs to ambient environments, substantial techniques have been proposed, such as lowering their dimensions[8-11], incorporating stable Cs^+ and Br^- ions[12] and coating them with protective layers[13,14].

In recent years, two-dimensional (2D) Ruddlesden-Popper perovskites, with large hydrophobic organic spacers inserted into the perovskite crystal lattices, have exhibited unique environmental and structural stability. Layered 2D Ruddlesden-Popper perovskites have a general formula of $A'_2A_{n-1}Pb_nX_{3n-1}X'_2$, where A' is a bulky organic cation spacer, A is a small-sized cation (FA^+, MA^+ and Cs^+), X and X' are the halide anions and n is an integer[15,16]. Ruddlesden-Popper perovskites with one layer of A' organic cations inserted into every n-layer of $[PbX_6]^{4-}$ octahedra are regarded as naturally formed quantum well structures, where the semiconductor three-dimensional (3D) layers correspond to the quantum wells and the organic spacer sheets act as barriers[17]. Owing to the structural versatility of the ammonium spacers, it is feasible to improve the photoresponse performance of 2D Ruddlesden-Popper PSCs by adjusting the structures of the organic spacer cations. Recently, several spacer ammoniums have been reported for 2D perovskite solar cells, such as benzylamine[18], phenylethylamine (PEA)[19,20], naphthalenemethylammonium[21] and thiophenemethylammonium[22]. Furthermore, it is also possible to further improve the hydrophobicity of 2D halide perovskites by adopting different ammonium spacers[23-26].

Liu *et al.* introduced a 2D A_2PbI_4 perovskite layer using pentafluorophenylethylammonium as a fluorine cation and the PSC devices produced reached a champion *PCE* of 22.2% with an open-circuit voltage (V_{OC}) of 1.096 V, which maintained 90% of its initial efficiency at a relative humidity (*RH*) of 40% after 1000 h[24]. Wang *et al.* reported halide substitution in phenethylammonium spacer cations, where F-PEA-based devices (n = 4) exhibited a champion *PCE* of 18.10% with the highest V_{OC} of 1.21 V and 80% of the initial *PCE* retained under 80 °C heating for 720 h[27]. Li *et al.* developed a hydrophobic 4-(trifluoromethyl)benzylamine as the spacer cations to induce a spontaneous upper gradient 2D structure and the devices (n = 60) exhibited a 17.07% *PCE* with a V_{OC} of 1.10 V and maintained 84% of the initial *PCE* in a N_2 box at room temperature[28]. Generally, fluorinated organics possess strong hydrophobicity and high electronegativity, but the thermal stability of fabricated PSCs with fluorine additives should be further improved and the potential of introducing 2D Ruddlesden-Popper perovskites still needs to be explored.

Herein, we demonstrate the preparation of a thermally stable quasi-2D perovskite by utilizing 3-(trifluoromethyl)benzylammonium iodide (3-TFMBAI) as a novel fluorinated spacer in $Cs_{0.17}FA_{0.83}Pb(I_{0.83}Br_{0.17})_3$. The constructed molecular planes of 3-(trifluoromethyl)benzylamine (3-TFMBA) cations have strong hydrophobicity against humidity, thus favorably suppressing the hydrolysis and decomposition of the perovskite phase in ambient air. Moreover, the introduction of 3-TFMBAI spacers leads to the formation of the Ruddlesden-Popper perovskite phase with quantum well structures that can passivate the trap states and restrain the ionic motion in the perovskite lattice. In addition, Cs^+ ions are adopted to increase the bandgap and improve the thermal stability of the prepared perovskite films. The as-prepared $(3\text{-}TFMBA)_2(Cs_{0.17}FA_{0.83})_{n-1}Pb_n(I_{0.83}Br_{0.17})_{3n-1}I_2$-based PSCs demonstrate a champion *PCE* of 20.89% and a high V_{OC} of 1.22 V at n = 40. The quasi-2D PSCs free of encapsulation demonstrate extraordinary performance regarding both thermal and moisture stability, preserving 90.7% of their initial efficiency after being continuously heated at 60 °C in humid air with a *RH* of 60% for 1000 h. This represents a significant improvement compared to previous works on other fluorine additives[24,27,28]. Finally, we couple the semi-transparent quasi-2D PSCs with monocrystalline silicon solar cells to fabricate four-terminal tandem solar cells, which achieve a total *PCE* of 23.53% and favorable device stability in ambient environments.

EXPERIMENTAL

Chemicals and materials. Formamidinium iodide (FAI, > 99%), 4-*tert*-butylpyridine (≥ 96.0%) and patterned fluorinated tin oxide (FTO) glass substrates were purchased from Advanced Election Technology Co., Ltd., China. Lead iodide (PbI_2, 99.9985%), bis(trifluoromethane)sulfonimide lithium salt (Li-TFSI, > 98%), SnO_2 colloidal solution (15 wt.% in a H_2O colloidal dispersion), *N,N*-dimethylformamide (DMF, 99.8%), chlorobenzene (99.8%) and acetonitrile (99.8%) were purchased from Alfa Aesar. Lead bromide ($PbBr_2$, 99.0%), cesium iodide (CsI, 99.999%), 3-TFMBA (98%), hydriodic acid (HI, *aq.*, 55.0-58.0%) and dimethyl sulfoxide (DMSO, 99.8%) were purchased from Aladdin Co., Ltd., China. The hole transfer material 2,2',7,7'-tetrakis(N,N-di-p-methoxyphenylamine)-9,9'-spirobifluorene (spiro-OMeTAD, > 99.8%) was purchased from Xi'an Polymer Light Technology Co., Ltd., China. All chemicals were used as received without further purification.

Synthesis of 3-TFMBAI. Briefly, 1520 mg (8.68 mmol) of 3-(trifluoromethyl)benzylamine were dissolved in 15.0 mL of ethanol and stirred at room temperature for 10 min. Then, 1800 μL of hydroiodic acid were added into the mixture and stirred at 50 °C for 2 h. Afterwards, the mixture was concentrated by rotary evaporation and washed with excessive diethyl ether. Finally, the precipitate was dried under vacuum to obtain a crystalline solid with a bright white color (2328 mg, 7.68 mmol and 88.5% yield).

Preparation of SnO_2 layer on FTO glass substrates. The patterned FTO glass substrates were sequentially cleaned by ultrasonication in acetone, ethanol and pure water for 15 min. The substrates were then treated with ultraviolet (UV)/ozone for 1 min at 60% power to remove the last traces of organic residues. Afterwards, a thin SnO_2 layer was deposited on the substrates by spin coating a diluted SnO_2 colloidal solution (4 wt.% in a H_2O colloidal dispersion) at 3000 rpm for 30 s, followed by annealing in air at 125 °C for 30 min. Finally, the above spin-coating and annealing procedures were repeated once more to obtain the SnO_2/FTO substrates.

Preparation of $(3\text{-}TFMBA)_2(Cs_{0.17}FA_{0.83})_{n-1}Pb_n(I_{0.83}Br_{0.17})_{3n-1}I_2$ perovskite layers. All the fabrication steps for the $(3\text{-}TFMBA)_2(Cs_{0.17}FA_{0.83})_{n-1}Pb_n(I_{0.83}Br_{0.17})_{3n-1}I_2$ perovskite layer were performed in a N_2-filled glovebox. For the sample with n = 40, a precursor mixture of 447.8 mg (0.971 mmol) of PbI_2, 120.6 mg (0.329 mmol) of $PbBr_2$, 180.9 mg (1.052 mmol) of FAI, 56.0 mg (0.215 mmol) of CsI and 19.7 mg (0.065 mmol) of 3-TFMBAI was dissolved in a 1 mL mixed solvent of DMF/DMSO (7:3 in volume) and stirred at room

temperature for 2 h. Then, 50 μL of the above mixed solution were deposited on the SnO_2/FTO substrate by spin coating at 6000 rpm for 30 s and 200 μL chlorobenzene was dropped at the 20th s. Subsequently, the films were annealed on a hotplate at 100 °C for 40 min to obtain the black perovskite layer. For the samples with n = 1, 4 and ∞, the total Pb^{2+} concentration was 1.3 M and the amount of each precursor was determined by the molar ratio of the chemical formula of $(3\text{-TFMBA})_2(Cs_{0.17}FA_{0.83})_{n-1}Pb_n(I_{0.83}Br_{0.17})_{3n-1}I_2$ with different n values, respectively.

Preparation of hole transport layers and counter electrodes. The spiro-OMeTAD solution was prepared by dissolving 80 mg of spiro-OMeTAD in 1 mL of chlorobenzene, followed by the addition of 17.5 μL of Li-TFSI (pre-dissolved in acetonitrile as a 520 mg/mL stock solution) and 28.8 μL of 4-*tert*-butylpyridine. Then, 35 μL of the as-prepared spiro-OMeTAD solution was deposited on the perovskite film by spin coating at 3000 rpm for 30 s. Finally, gold counter electrodes with a thickness of 10, 20, 30 or 40 nm were deposited by thermal evaporation at a rate of 0.3 Å/s to form the whole PSC device.

Fabrication of single-crystalline silicon solar cells. 170 μm-thick p-type monocrystalline silicon solar cells with the structure of a passivated emitter and rear cell (PERC) were fabricated via a standard industrial process. In this kind of cell, the front surface of c-Si was texturized with randomly distributed pyramids by a standard industrial wet etching method. The front antireflection coating of the standard PERC cell adopted a single-layer SiN_x thin film. Here, a thickness of 77 nm and a refractive index of 2.09 (at the wavelength of 630 nm) were chosen for the front SiN_x thin film. At the rear side, Al_2O_3 and SiN_x thin films were used for standard PERC cells. Here, the thicknesses of the Al_2O_3 and SiN_x thin films were set as 10 and 125 nm, respectively. A front emitter was conducted via high-temperature diffusion as a typical method to form a p-n junction. The front selective emitter was included under the front contacts. A local back surface field was applied to the rear side to improve the V_{OC}.

Materials characterization. The XRD patterns of the perovskite films were obtained using a Bruker D-8 Advance diffractometer with a Cu Kα X-ray source. XPS analyses were carried out with a PHI-5000 VersaProbe X-ray photoelectron spectrometer with an Al Kα X-ray source. UV-vis absorbance spectra were measured by a Shimadzu UV-2456 spectrophotometer. The PL spectra and decay curves of the perovskite layer on the SnO_2/FTO substrate were recorded on a home-built wide-field fluorescence microscope under an excitation wavelength of 450 nm. Both the top-view and cross-sectional SEM images were obtained with a FEI Nano Nova-450 instrument.

Photovoltaic measurements. Before the photovoltaic tests, the PSCs were illuminated under simulated AM 1.5 G solar light using a solar simulator (100 mW/cm², NOWDATA SXDN-150E) for 15 min in advance for activation. The *J-V* curves were measured with a Keithley 2400 Source Meter under a simulated AM 1.5 G illumination. The light intensity was calibrated with a standard single-crystalline Si solar cell. Both the forward and reverse scans were measured with a scanning speed of 200 mV/s.

RESULTS AND DISCUSSION

The 3-TFMBAI additive in the form of a crystalline bright white powder was synthesized by the reaction of 3-TFMBA and hydroiodic acid in ethanol, as presented in the Experimental section and Supplementary Figure 1. Supplementary Figure 2 shows the Fourier transform infrared spectra of the 3-TFMBA precursor and as-synthesized 3-TFMBAI product. The strong, wide and dispersed absorption bands between 2700 and 3200 cm^{-1} were assigned to the stretching vibration absorption of the N-H bond in the $-NH_3^+$ group, which indicates the successful synthesis of 3-TFMBAI. 3-TFMBAI was then added to a mixture of PbI_2, $PbBr_2$, FAI and CsI in a mixed DMF/DMSO solvent (7:3 in volume) under stirring. The

mixed precursor solution was deposited on a SnO_2-coated FTO glass substrate and dropped with 200 μL of chlorobenzene. Subsequently, the substrates were annealed at 100 °C to obtain the black quasi-2D perovskite films.

Figure 1A shows the crystalline structure of $(3\text{-TFMBA})_2(Cs_{0.17}FA_{0.83})_{n-1}Pb_n(I_{0.83}Br_{0.17})_{3n-1}I_2$ perovskites, where the perovskite layers are sandwiched between the molecular planes composed of 3-TFMBA. Figure 1B shows the XRD characterization of the perovskite films. When $n = 1$, the perovskite film is a pure 2D phase with the XRD peaks indexed to the planes of (002), (004), (006), (008) and so on. In addition to the characteristic peaks of the 2D phase, the peaks of the (110), (220) and (314) planes, which belong to the 3D phase, appear in the XRD pattern of the perovskite with $n = 4$. As the value of n increases to 40 and then ∞, the XRD patterns are dominated by the peaks of the 3D phase, which are located at 14.16°, 20.11°, 24.62°, 28.50°, 31.98°, 40.83° and 43.36°, corresponding to the (110), (012), (013), (220), (310), (224) and (314) planes of the perovskite phase, respectively.

After normalizing the XRD patterns of the perovskite samples with $n = 40$ and ∞ according to the strongest peak of the (110) planes, it is found that the full width at half maximum (FWHM) of the sample with $n = 40$ (0.145°) is smaller than that of the sample with $n = ∞$ (0.162°). This confirms that introducing a small amount of 3-TFMBAI into the perovskite bulk phase to form a molecular plane could indeed increase the overall crystallinity of the perovskite film due to the orientation effects of the amino hydrogen bonds (N-H··· X, X = I or Br) between the ammonium cations of 3-TFMBA$^+$ and $[PbX_6]^{4-}$ (X = I or Br) octahedral frameworks during the annealing process[29]. Scanning electron microscopy (SEM) was performed to investigate the surface morphology of the perovskite samples with $n = 40$ and ∞. Compared to the samples with $n = 4$ [Supplementary Figure 3A and B] and ∞ [Supplementary Figure 3D and E], the perovskite film with $n = 40$ [Figure 1C and Supplementary Figure 3C] presented a smoother and more compact surface with a uniform and large grain size of ~500 nm within a large area. For the sample with $n = ∞$ (without the addition of 3-TFMBAI), a small number of pinholes and cracks caused by the sublimation of FAI during the annealing preparation process was observed [Supplementary Figure 3D and E], leading to charge recombination and a slight loss in the V_{OC} of the PSCs. In contrast, the introduction of the 3-TFMBAI additive can make up for the vacancies generated by FAI sublimation [Supplementary Figure 3C], thereby improving the boundary contact of crystal grains and the integrity of the entire perovskite film.

XPS analysis was performed to identify the chemical compositions of the prepared perovskite films with different n values [Figure 1D-I]. After setting the C 1s peak of adventitious carbon to 284.8 eV, the high-resolution XPS spectra of the Br 3d, I 3d, Pb 4f, Cs 3d and F 1s bands were collected [Figure 1E-I] and the characteristic binding energies of these elements are summarized in Supplementary Table 1. Figure 1H and I show the high-resolution XPS spectra of the Cs 3d and F 1s peaks, indicating the formation of a bi-cation organic-inorganic perovskite layer and the introduction of 3-TFMBAI. When the n value increases, it can be seen that the Cs 3d peaks become stronger, while the intensity of the F 1s peak is reduced, which is consistent with the change in the amounts of CsI and 3-TFMBAI precursors used in the experimental process. Moreover, as the n value increased from 1 to ∞, the intensities of the Br 3d and Cs 3d peaks became higher, while the intensities of the I 3d and F 1s peaks decreased, consistent with the variations in the amounts of PbI_2, $PbBr_2$, FAI, CsI and 3-TFMBAI precursors used in the experimental process. The corresponding XPS peak area and atomic concentration of each element are summarized in Supplementary Table 2.

Furthermore, the ammonium cation in 3-TFMBA$^+$ can form a hydrogen bond with the Br$^-$ ion (N-H··· Br) in the $[PbI_5Br]^{4-}$ octahedral framework in the perovskite lattice[29], which weakens the originally strong
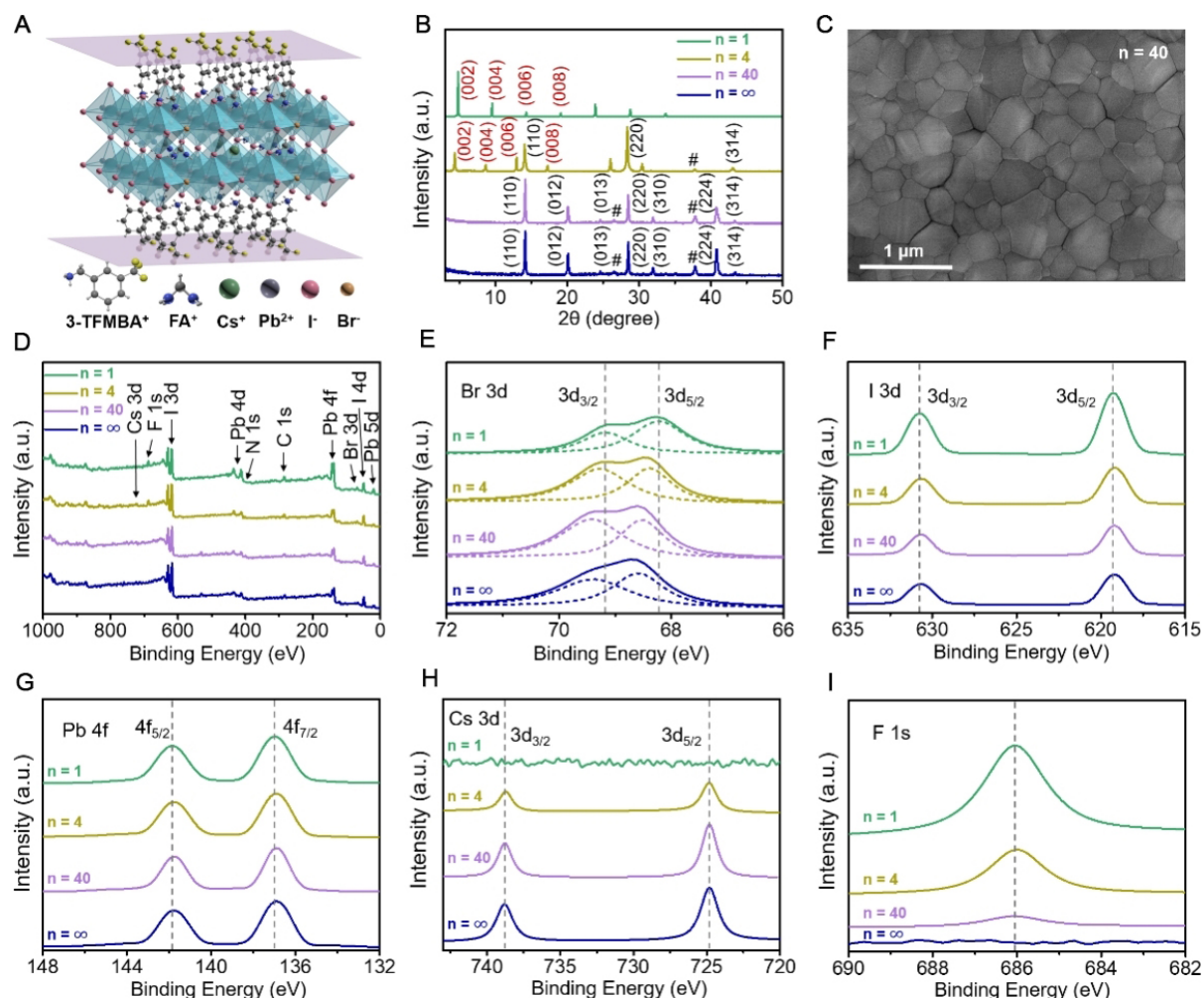
Figure 1. Structural and compositional analyzes of as-prepared perovskite films. (A) Crystalline structure of $(3\text{-TFMBA})_2(Cs_{0.17}FA_{0.83})_{n-1}Pb_n(I_{0.83}Br_{0.17})_{3n-1}I_2$ perovskite. (B) XRD patterns (peaks labeled with "#" are derived from FTO). (C) Top-view SEM image of quasi-2D perovskite film with $n = 40$. (D) Survey XPS spectra and (E-I) corresponding high-resolution XPS spectra at (E) Br 3d, (F) I 3d, (G) Pb 4f, (H) Cs 3d and (I) F 1s regions of quasi-2D perovskite films with different n values.

chemical interaction between Pb^{2+} and Br^-, resulting in the shift of the Br 3d band position to lower binding energy with increasing 3-TFMBAI concentration. Due to the small electronegativity of I ($EN_I = 2.5$, similar to carbon), the hydrogen bond between an I^- ion and an ammonium cation is very weak, so the doping of 3-TFMBAI has little influence on the XPS binding energy of the I 3d band. As there is no A-site cation (FA^+ and Cs^+) in the perovskite film with $n = 1$ but only strong chemical bonding between I^- and Pb^{2+}, the XPS binding energies of the I 3d and Pb 4f bands in the perovskite film with $n = 1$ are slightly higher than those with other n values (i.e., $n = 4$, 40 and ∞)[30].

To verify the presence of 2D and quasi-2D structures, the ultraviolet–visible spectroscopy (UV-Vis) absorption spectra of the perovskite films with different n values were measured, as shown in Figure 2A. The perovskite films with $n = 1$ and 2 clearly exhibit strong absorption peaks at 488 and 549 nm derived from the Stage-1 and Stage-2 intercalations of 3-TFMBA, respectively, where Stage-x represents x layers of $[PbI_5Br]^{4-}$ octahedra sandwiched between each two 3-TFMBA molecular planes. These results indicate that the introduction of 3-TFMBAI can form a low-dimension Ruddlesden-Popper structure in the perovskite
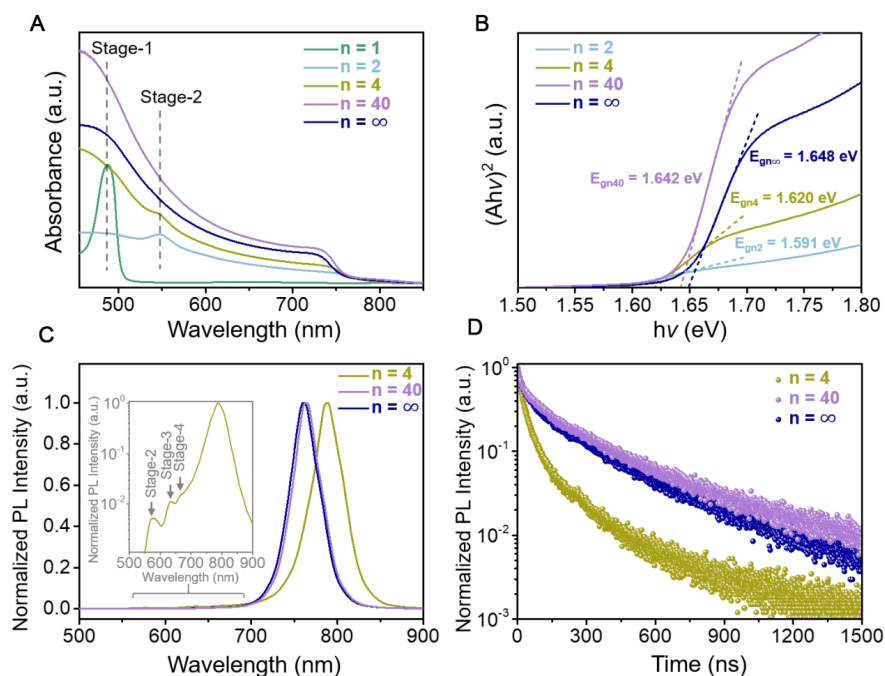
Figure 2. Photoresponse properties of as-prepared perovskite films. (A) UV-Vis absorption spectra (in which Stage-x represents x layers of $[PbI_5Br]^{4-}$ octahedra sandwiched between each two 3-TFMBA molecular planes), (B) corresponding $(Ah\nu)^2$ *vs. h\nu* curves, (C) steady PL spectra and (D) TRPL spectra of $(3\text{-TFMBA})_2(Cs_{0.17}FA_{0.83})_{n-1}Pb_n(I_{0.83}Br_{0.17})_{3n-1}I_2$ perovskite films.

layers. The absorption peaks of the Stage-3 and Stage-4 intercalations are not so obvious, mainly because the perovskite layer with FA^+ as the A site would exhibit a suppressed absorption peak of low-n phases[31]. When the *n* values increase to 40 and ∞, there is no such obvious low-dimensional absorption peak in the absorption curves and the 3D phase absorption edges were at 755 and 752 nm, respectively. Figure 2B shows the bandgap values calculated from the UV-Vis absorption spectra of the perovskite films with different *n* values. Unsurprisingly, the increase in the Br/I element ratio leads to a decrease in the absorption range, while the samples with large *n* values present relatively large bandgaps (1.591 eV for *n* = 2, 1.620 eV for *n* = 4, 1.642 eV for *n* = 40 and 1.648 eV for *n* = ∞).

Similar to the UV-Vis absorption spectra, the perovskite films with *n* = 4, 40 and ∞ exhibited strong 3D phase PL emission peaks at 789, 763 and 761 nm, respectively, as shown in Figure 2C. By comparing the FWHM of these peaks (45.3 nm for *n* = 4, 40.7 nm for *n* = 40 and 41.6 nm for *n* = ∞), it can be found that the perovskite film with *n* = 40 has the smallest FWHM value, indicating the highest crystal quality, as also indicated by the previous XRD patterns and SEM results. After logarithmic transformation of the ordinate, small PL emission peaks of low-n phases can be clearly observed, as shown in the inset of Figure 2C. Time-resolved PL (TRPL) spectroscopy was carried out to explore the charge-recombination kinetics in perovskite films with different *n* values [Figure 2D]. The curves were fitted by the following bi-exponential decay function[32]:

$$f(t) = A_1 e^{-t/\tau_1} + A_2 e^{-t/\tau_2} \tag{1}$$

where the measured parameters A_1, A_2, τ_1 and τ_2 of different *n* values are summarized in Supplementary Table 3. The average lifetime of the perovskite film with *n* = 40 (91 ns) is longer than those of *n* = 4 (35 ns) and ∞ (87 ns), which demonstrates that a small amount of 3-TFMBAI additive can reduce
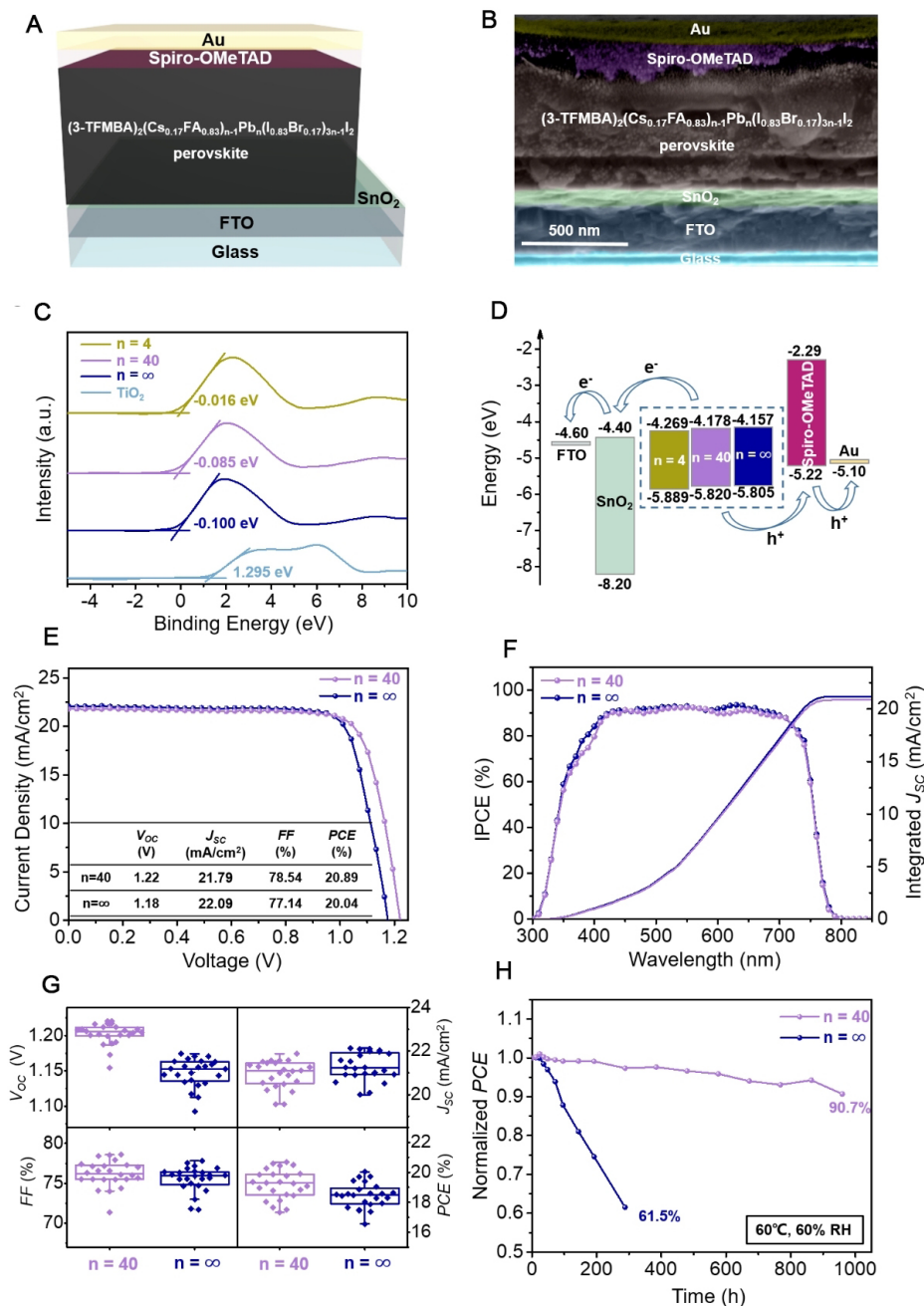
Figure 3. Device configuration and photovoltaic performance of PSCs. (A) Schematic structure and (B) cross-sectional SEM image of PSCs with glass/FTO/SnO_2/perovskite/spiro-OMeTAD/80-nm-Au configuration. (C) Valence-band XPS spectra and (D) corresponding energy level alignment diagrams. (E) Typical *J-V* plots, (F) IPCE spectra and (G) box diagrams of V_{OC}, J_{SC}, *FF* and *PCE* distributions of 24 individual PSCs with different *n* values. (H) Normalized *PCE* retentions of different PSCs without encapsulation under continuous heating at 60 °C and simultaneous exposure to humid air with a *RH* of 60%.

the trap density in the perovskite film, resulting in a relatively lower recombination rate of the photogenerated carriers.

The perovskite films were then applied in PSCs with the device configuration of glass/FTO/SnO$_2$ /perovskite/spiro-OMeTAD/80-nm-Au [Figure 3A], corresponding to the layers exhibited in the cross-sectional SEM image of Figure 3B. Valence-band XPS tests were carried out to determine the energy band levels of perovskites with different *n* values [Figure 3C]. As the valence band maximum (VBM) of the standard TiO$_2$ sample can be determined to -7.2 eV[33], the VBM of the perovskites with *n* = 4, 40 and ∞ can be calculated as -5.889, -5.820 and -5.805 eV, respectively. Furthermore, the UV-Vis absorption spectra [Figure 2A and B] confirm the optical bandgaps, so the conduction band minimum (CBM) of the perovskites with *n* = 4, 40 and ∞ can be calculated as -4.269, -4.178 and -4.157 eV accordingly. Hence, the energy band levels of each functional layer in the whole device are summarized in Figure 3D, which associates the electron extraction from the CBM of the perovskite to that of the SnO$_2$ electron transfer layer and the hole extraction from the VBM of perovskite to that of the spiro-OMeTAD hole transfer layer.

Figure 3E and Supplementary Figure 4 show the *J-V* plots of PSCs with different *n* values and the corresponding photovoltaic parameters. The short-circuit current density (J_{SC}) of the PSC with *n* = 40 (21.79 mA/cm^2) was slightly lower than that of the PSC with *n* = ∞ (22.09 mA/cm^2). Since the dipole moment of the 3-TFMBA$^+$ cation is much larger than that of chlorobenzene [Supplementary Figure 5], it is more difficult to spin coat the solution of chlorobenzene containing spiro-OMeTAD on the surface of the perovskite film with *n* = 40. Therefore, the perovskite material with *n* = ∞ exhibits better contact with the hole transfer layer, finally resulting in a slight decrease in the J_{SC} of the PSC with increasing 3-TFMBAI doping concentration. Importantly, due to the increase in the bandgap and the improvement in the grain boundaries resulting from 3-TFMBAI doping, the V_{OC} of the PSC with *n* = 40 reaches 1.22V, which is the highest among the previous works on fluorine additives[23-28], finally resulting in a high *PCE* of 20.89%.

Incident photon-to-electron conversion efficiency (IPCE) measurements were carried out to validate the current densities of the PSCs with *n* = 40 and ∞ [Figure 3F]. Similar to the UV-Vis absorption and PL spectra, the IPCE onset wavelengths are ~780 nm and the quantum efficiency values from 400 to 740 nm are over 80%. The integrated J_{SC} values of the PSCs with *n* = 40 and ∞ are calculated to be 20.87 and 21.20 mA/cm^2, respectively, in good agreement with the J_{SC} values measured under AM 1.5 G illumination [Figure 3E]. Electrochemical impedance spectroscopy was conducted to further elucidate the positive effect of 3-TFMBAI doping on the charge transport properties of the PSCs, as shown in Supplementary Figure 6. The PSC with *n* = 40 exhibits lower charge transfer resistance (R_{tr}) and higher carrier recombination resistance (R_{rec}) than those of the PSC with *n* = ∞, indicating optimized charge transport and suppressed charge recombination[34]. Figure 3G shows the distributions of the V_{OC}, J_{SC}, *FF* and *PCE* of PSCs with *n* = 40 and ∞, verifying the high repeatability of the device fabrication process. The average *PCE* of 24 individual PSCs with *n* = 40 (19.18%) was higher than that of the PSCs with *n* = ∞ (18.46%), with the detailed data summarized in Supplementary Table 4.

The long-term stability tests of PSCs with *n* = 40 and ∞ free of any encapsulation were carried out by heating at 60 °C and exposure to humid air with a *RH* of 60% [Figure 3H]. After being continuously heated at 60 °C for 960 h, the PSCs with *n* = 40 still maintained 90.7% of their initial *PCE*, which was significantly better than that of the PSCs with *n* = ∞ (61.5% after 288 h). To further illustrate the effect of 3-TFMBAI doping on the thermal and moisture stability of the PSCs, XRD analysis of the perovskite films [Supplementary Figure 7] and stability tests of the PSC devices were synchronously performed. Due to the collapse of the perovskite phase with *n* = ∞ induced by heat and humidity, the intensity of the PbI$_2$ peak at 12.67° increases gradually, leading to charge recombination at the grain boundaries of the perovskite film, finally resulting in a decrease in the J_{SC} and *FF* parameters of the PSC devices [Supplementary Figure 8]. However, since the strong hydrogen bond (F⋯N-H) between 3-TFMBA$^+$ and FA$^+$ can effectively suppress

the decomposition of the perovskite[28], the V_{OC}, J_{SC} and *FF* parameters of PSCs with $n = 40$ still maintained a high retention ratio after the stability test for 1000 h.

Contact angle measurements were carried out to further investigate the improvement in the humidity resistance of the perovskite films with the introduction of 3-TFMBAI, as shown in Supplementary Figure 9. The perovskite film with $n = 40$ exhibits a larger contact angle (62.2°) than the perovskite film with $n = \infty$ (56.8°). With the further increase in 3-TFMBAI doping concentration ($n = 4$), the contact angle continued to become larger as well (71.1°). These results could be attributed to the strong hydrophobicity of the 3-TFMBA molecular plane, which could prevent humidity from penetrating into the perovskite layer, thus greatly improving the moisture resistance of the fabricated PSCs. These results suggest that the PSCs with $n = 40$ have better thermal and moisture stability than those with $n = \infty$, because the doping of 3-TFMBAI can effectively restrain the ionic motion in the perovskite lattice and suppress the decomposition of the perovskite phase against heat and humidity.

To study the effects of the 3-TFMBAI doping concentration on the crystalline structure and photoresponse properties, $(3\text{-TFMBA})_2(Cs_{0.17}FA_{0.83})_{n-1}Pb_n(I_{0.83}Br_{0.17})_{3n-1}I_2$ perovskite films with different n values ($n = 10, 20, 40$ and 60) were prepared [Figure 4]. The XRD patterns [Figure 4A] of the perovskites are all dominated by the peaks of the 3D perovskite phase. After normalizing the XRD patterns according to the strongest peaks of the (110) planes, it is found that the FWHM of the perovskite film with $n = 40$ is the smallest (0.164° for $n = 10$, 0.156° for $n = 20$, 0.145° for $n = 40$ and 0.149° for $n = 60$), indicating that is has the best crystallinity. These results suggest that the doping ratio of 3-TFMBAI should be moderate at most, because excessive 3-TFMBAI doping may deform the crystal structure and insufficient 3-TFMBAI doping cannot fully address the lattice defects generated by FAI sublimation during the annealing process[35]. Figure 4B shows the UV-Vis absorption spectra of the perovskite films with different n values. It can be clearly seen that the perovskite film with $n = 40$ has the strongest absorption intensity. Similar to Figure 2A, as the n value increases, the absorption edge of the UV-Vis absorption curve is continuously blue shifted, resulting in a slight increase in the bandgap of the perovskite films, as illustrated in the $(Ah\nu)^2$-$h\nu$ curves of Figure 4C (1.630 eV for $n = 10$, 1.635 eV for $n = 20$, 1.642 eV for $n = 40$ and 1.646 eV for $n = 60$). Similar to Figure 3E, the J_{SC} of the PSC with $n = 40$ (21.79 mA/cm²) is slightly lower than that of the PSC with $n = 60$ (21.98 mA/cm²). However, the higher crystallinity, better boundary conditions and stronger light absorption greatly improved the V_{OC} and *FF* of the PSC with $n = 40$ [Figure 4D], leading to the highest photoelectric conversion efficiency. The detailed photovoltaic parameters are compared in Supplementary Table 5.

For the assembly of four-terminal tandem solar cells, semi-transparent PSCs were stacked with a p-type monocrystalline silicon solar cell, as displayed in Figure 5A. The bottom silicon solar cell with the PERC structure was fabricated via a standard industrial process, as detailed in the Experimental section. The insets of Figure 5B exhibit the cross-sectional structure and photovoltaic parameters of the bottom silicon solar cell. The *J-V* response of this silicon PERC solar cell was tested and the J_{SC}, V_{OC} and *FF* values were measured to be 40.29 mA/cm², 0.680 V and 80.59%, respectively, corresponding to a photoelectric conversion efficiency of 22.09%.

In the four-terminal tandem solar cell, the top semi-transparent PSC absorbs most of the sunlight in the visible region, with most of the near-infrared light not absorbed. The near-infrared light passes through the PSC and illuminates the bottom silicon solar cell. Therefore, it is important to improve the transmittance of the top PSC in the near-infrared region (800-1200 nm), which is the main light absorption region of silicon solar cells. Notably, the perovskite layer has little absorption in the near-infrared region [Supplementary Figure 10] and thus the thickness of the gold counter electrode plays a crucial role in the
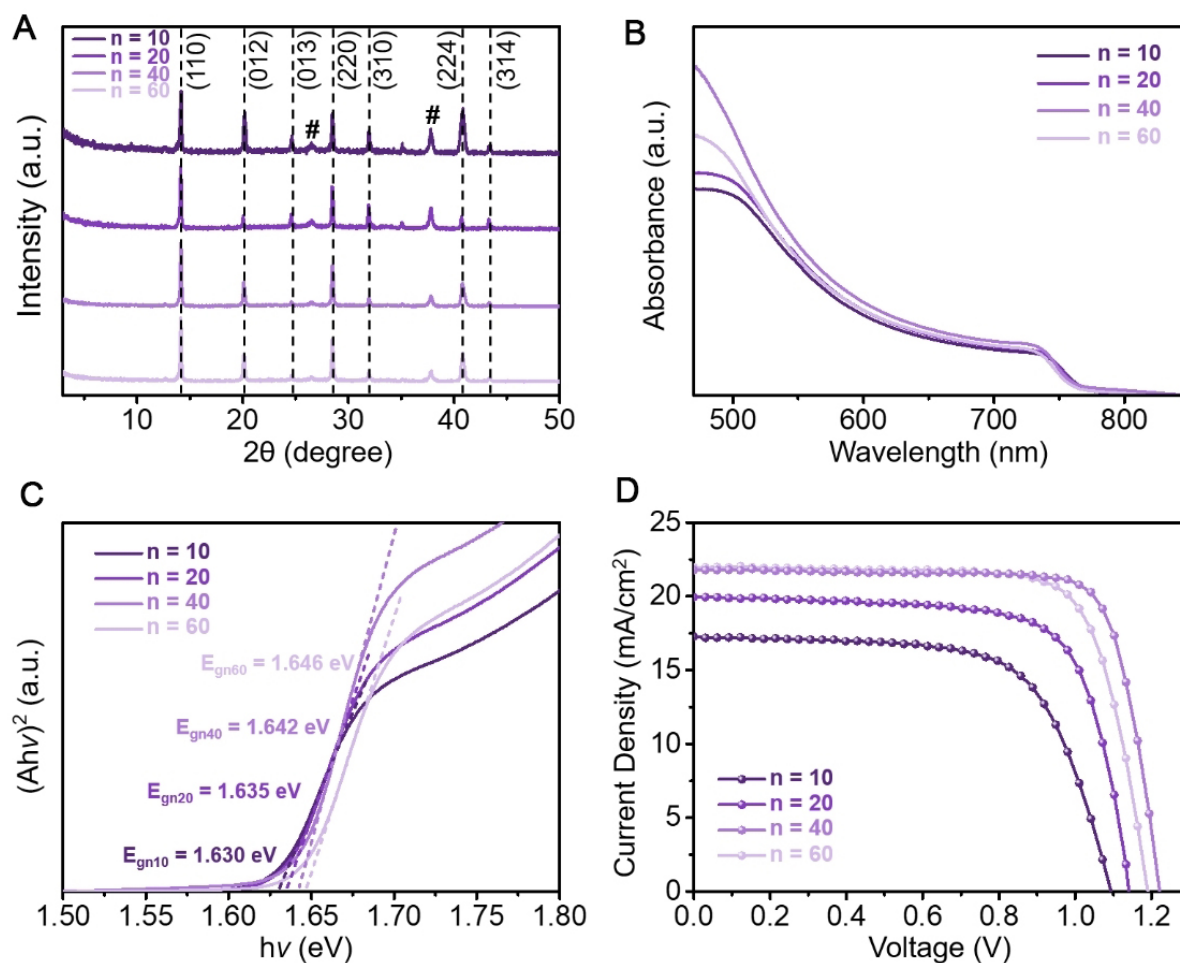
Figure 4. Structural and photoresponse influences of 3-TFMBAI doping ratios. (A) XRD patterns (peaks labeled with "#" are derived from FTO), (B) UV-vis spectra, (C) $(Ah\nu)^2$ vs. $h\nu$ curves and (D) typical *J-V* plots of quasi-2D perovskites with different 3-TFMBAI doping concentrations (n = 10, 20, 40 and 60).

transmittance of the entire PSC in the near-infrared region. The influences of the different thicknesses of the Au counter electrode on the near-infrared transmittance and internal resistance of the top PSC were investigated, as summarized in Figure 5C and D and Supplementary Table 6. With the 10 nm-thick Au electrode, the average transmittance of the PSC in the near-infrared region exceeds 32%, but the internal resistance of the device is too large to obtain a satisfactory *PCE*. With 20, 30 and 40 nm-thick gold electrodes, the internal resistance slightly decreases, but the average transmittance in the near-infrared region drops significantly. Therefore, a 20 nm-thick Au counter electrode was adopted to achieve the best performance of the four-terminal tandem solar cells.

When assembled in four-terminal tandem solar cells, the top PSC (with n = 40 and a 20 nm-thick Au electrode) exhibited a champion *PCE* of 19.11% while the bottom silicon solar cell exhibited a champion *PCE* of 4.42%. The *J-V* curves and detailed photovoltaic parameters of these two parts are shown in Figure 5E and Supplementary Table 7, respectively. As a result, the total champion *PCE* of the whole four-terminal tandem solar cells reached 23.53%. For comparison, Figure 5F shows the distributions of the V_{OC}, J_{SC}, *FF* and *PCE* values of the top PSCs with n = 40 and ∞ based on 20 nm-thick Au electrodes, verifying the high repeatability of the fabrication process. The average *PCE* of 48 individual PSCs with n = 40 (17.54%)
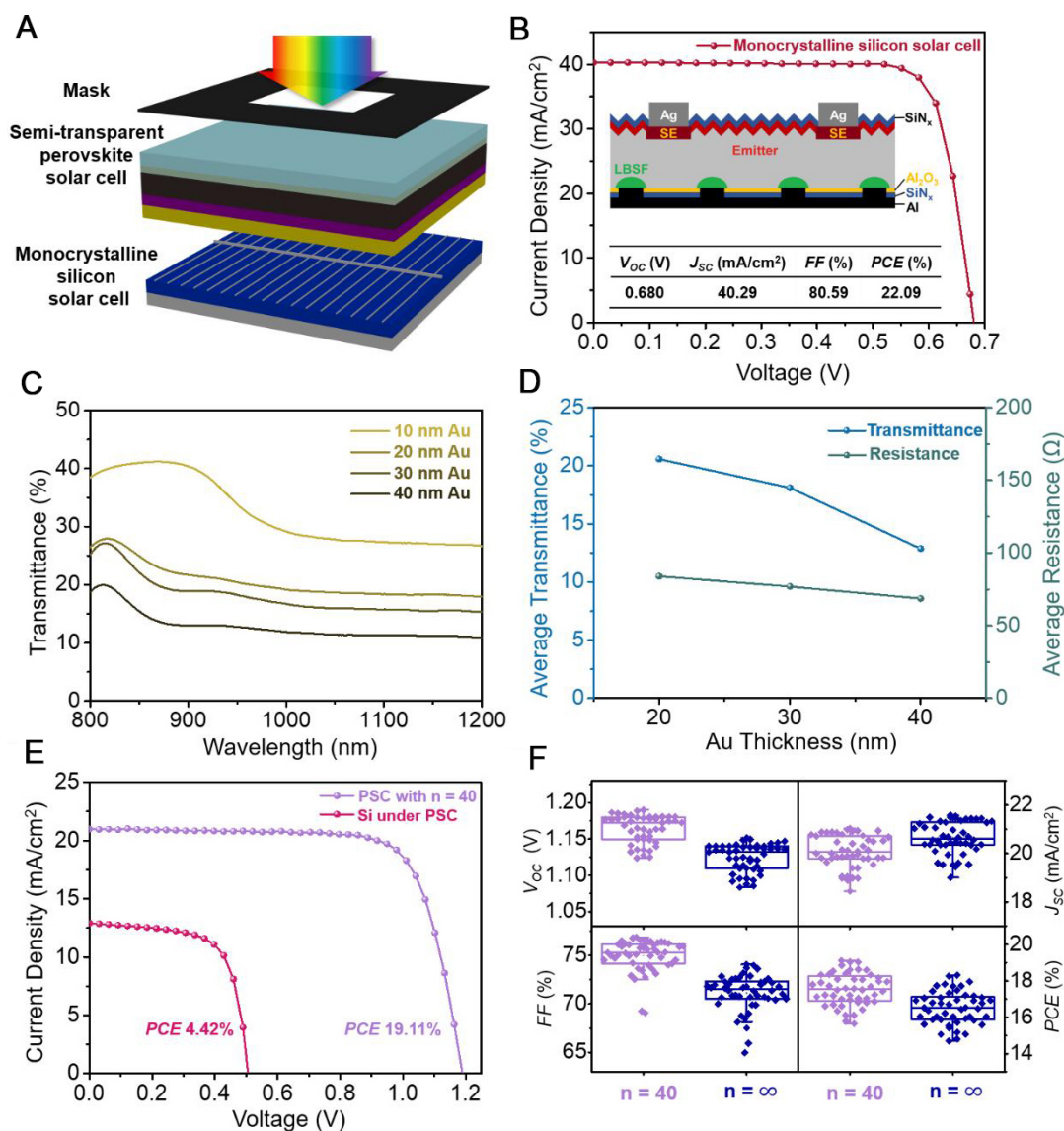
Figure 5. Device configuration and performance of silicon solar cells and four-terminal tandem solar cells. (A) Device configuration of a four-terminal tandem solar cell stacked by a top PSC and a bottom silicon solar cell. (B) *J-V* plots of monocrystalline silicon solar cells, where the insets are the cross-sectional structure and corresponding photovoltaic parameter values. (C) Near-infrared transmittance and (D) average transmittance and internal resistance of PSCs with different thicknesses of Au counter electrodes. (E) *J-V* plots of top PSC with *n* = 40 and bottom silicon solar cell. (F) Box diagrams of *VOC, JSC, FF* and *PCE* distributions of 48 PSCs with different *n* values based on 20 nm-thick Au counter electrodes.

was higher than that of the PSCs with $n = \infty$ (16.52%) and the detailed data are summarized in Supplementary Tables 8 and 9, further confirming that $n = 40$ is the most favorable doping ratio of the 3-TFMBAI additive for quasi-2D $(3\text{-TFMBA})_2(Cs_{0.17}FA_{0.83})_{n-1}Pb_n(I_{0.83}Br_{0.17})_{3n-1}I_2$ PSCs.

CONCLUSIONS

In summary, we have reported the preparation of a novel quasi-2D perovskite phase with improved absorbance, crystallinity and moisture stability via a one-step anti-solvent process by introducing a novel fluorinated additive (3-TFMBAI) into $Cs_{0.17}FA_{0.83}Pb(I_{0.83}Br_{0.17})_3$. This small fluorinated organic ammonium

molecule could compensate for the pinholes and cracks in the perovskite during the annealing process and thus achieve a high-quality perovskite film with larger grain sizes and reduced crystalline defect densities. Furthermore, the moderate doping of 3-TFMBAI efficiently tuned the bandgap of the perovskite film, so that the V_{OC} of the fabricated PSC increased to 1.22 V with a champion *PCE* of 20.89%. Moreover, the strongly hydrophobic 3-TFMBAI additive could help block water molecules and suppress the moisture/heat decomposition of the perovskite, resulting in an excellent performance stability of PSCs without encapsulation under long-term high-temperature heating in humid air. Finally, the semi-transparent quasi-2D PSCs were coupled with monocrystalline silicon solar cells to construct four-terminal tandem solar cells, achieving an overall *PCE* of 23.53% and favorable device stability. This work helps to tackle the intractable issue regarding the intrinsic thermal and moisture instability of organic-inorganic hybrid perovskite materials through the doping of small fluorinated organic molecules and provides a novel prototype design for future tandem solar cells for all seasons.

DECLARATIONS

Authors' contributions
Conceived the idea of this study and designed the experiments: Jin Z, Xia Y, Zhu M
Performed the material synthesis: Xia Y, Zhu M
Contributed to the XRD, SEM, IPCE, UV and XPS characterization: Xia Y, Zhu M, Qin L
Fabricated the solar cells and tested the photovoltaic performances: Xia Y, Zhu M, Zhao C
Carried out the PL characterizations: Hong D, Tian Y
Analyzed the data and wrote the paper: Jin Z, Xia Y, Zhu M
Supervised this project: Jin Z, Yan W

Availability of data and materials
The data that support the findings of this study are available from the corresponding author upon reasonable request.

Financial support and sponsorship

Conflicts of interest
All authors declared that there are no conflicts of interest.

Ethical approval and consent to participate
Not applicable.

Consent for publication
Not applicable.

Copyright

© The Author(s) 2023.

REFERENCES

1. De Wolf S, Holovsky J, Moon SJ, et al. Organometallic halide perovskites: sharp optical absorption edge and its relation to photovoltaic performance. *J Phys Chem Lett* 2014;5:1035-9. DOI
2. Kim G, Petrozza A. Defect tolerance and intolerance in metal-halide perovskites. *Adv Energy Mater* 2020;10:2001959. DOI
3. McMeekin DP, Sadoughi G, Rehman W, et al. A mixed-cation lead mixed-halide perovskite absorber for tandem solar cells. *Science* 2016;351:151-5. DOI PubMed
4. Stranks SD, Eperon GE, Grancini G, et al. Electron-hole diffusion lengths exceeding 1 micrometer in an organometal trihalide perovskite absorber. *Science* 2013;342:341-4. DOI PubMed
5. Kojima A, Teshima K, Shirai Y, Miyasaka T. Organometal halide perovskites as visible-light sensitizers for photovoltaic cells. *J Am Chem Soc* 2009;131:6050-1. DOI PubMed
6. Min H, Lee DY, Kim J, et al. Perovskite solar cells with atomically coherent interlayers on SnO_2 electrodes. *Nature* 2021;598:444-50. DOI PubMed
7. Zhang X, Ren X, Liu B, et al. Stable high efficiency two-dimensional perovskite solar cells via cesium doping. *Energy Environ Sci* 2017;10:2095-102. DOI
8. Cao DH, Stoumpos CC, Farha OK, Hupp JT, Kanatzidis MG. 2D homologous perovskites as light-absorbing materials for solar cell applications. *J Am Chem Soc* 2015;137:7843-50. DOI PubMed
9. Quan LN, Yuan M, Comin R, et al. Ligand-stabilized reduced-dimensionality perovskites. *J Am Chem Soc* 2016;138:2649-55. DOI PubMed
10. Stoumpos CC, Cao DH, Clark DJ, et al. Ruddlesden-popper hybrid lead iodide perovskite 2D homologous semiconductors. *Chem Mater* 2016;28:2852-67. DOI
11. Tsai H, Nie W, Blancon JC, et al. High-efficiency two-dimensional Ruddlesden-Popper perovskite solar cells. *Nature* 2016;536:312-6. DOI PubMed
12. Liang J, Wang C, Wang Y, et al. All-inorganic perovskite solar cells. *J Am Chem Soc* 2016;138:15829-32. DOI
13. Bella F, Griffini G, Correa-Baena JP, et al. Improving efficiency and stability of perovskite solar cells with photocurable fluoropolymers. *Science* 2016;354:203-6. DOI PubMed
14. Zhu H, Ren Y, Pan L, et al. Synergistic effect of fluorinated passivator and hole transport dopant enables stable perovskite solar cells with an efficiency near 24%. *J Am Chem Soc* 2021;143:3231-7. DOI PubMed
15. Leng K, Abdelwahab I, Verzhbitskiy I, et al. Molecularly thin two-dimensional hybrid perovskites with tunable optoelectronic properties due to reversible surface relaxation. *Nat Mater* 2018;17:908-14. DOI PubMed
16. Mao LL, Stoumpos CC, Kanatzidis MG. Two-dimensional hybrid halide perovskites: principles and promises. *J Am Chem Soc* 2019;141:1171-90. DOI PubMed
17. Xi J, Spanopoulos I, Bang K, et al. Alternative organic spacers for more efficient perovskite solar cells containing ruddlesden-popper phases. *J Am Chem Soc* 2020;142:19705-14. DOI PubMed
18. Zheng H, Liu G, Zhu L, et al. The effect of hydrophobicity of ammonium salts on stability of quasi-2D perovskite materials in moist condition. *Adv Energy Mater* 2018;8:1800051. DOI
19. Zhang J, Qin J, Wang M, et al. Uniform permutation of quasi-2D perovskites by vacuum poling for efficient, high-fill-factor solar cells. *Joule* 2019;3:3061-71. DOI
20. Zhao X, Liu T, Kaplan AB, Yao C, Loo YL. Accessing highly oriented two-dimensional perovskite films via solvent-vapor annealing for efficient and stable solar cells. *Nano Lett* 2020;20:8880-9. DOI PubMed
21. Xu Z, Lu D, Liu F, et al. Phase distribution and carrier dynamics in multiple-ring aromatic spacer-based two-dimensional ruddlesden-popper perovskite solar cells. *ACS Nano* 2020;14:4871-81. DOI PubMed
22. Lai H, Kan B, Liu T, et al. Two-dimensional ruddlesden-popper perovskite with nanorod-like morphology for solar cells with efficiency exceeding 15%. *J Am Chem Soc* 2018;140:11639-46. DOI PubMed
23. Lai H, Lu D, Xu Z, Zheng N, Xie Z, Liu Y. Organic-salt-assisted crystal growth and orientation of quasi-2D ruddlesden-popper perovskites for solar cells with efficiency over 19%. *Adv Mater* 2020;32:e2001470. DOI PubMed
24. Liu Y, Akin S, Pan L, et al. Ultrahydrophobic 3D/2D fluoroarene bilayer-based water-resistant perovskite solar cells with efficiencies exceeding 22%. *Sci Adv* 2019;5:eaaw2543. DOI PubMed PMC
25. Pan H, Zhao X, Gong X, Shen Y, Wang M. Atomic-scale tailoring of organic cation of layered ruddlesden-popper perovskite compounds. *J Phys Chem Lett* 2019;10:1813-9. DOI PubMed
26. Wei Y, Chen B, Zhang F, et al. Compositionally designed 2D ruddlesden-popper perovskites for efficient and stable solar cells. *Solar RRL* 2021;5:2000661. DOI
27. Wang Z, Wei Q, Liu X, et al. Spacer cation tuning enables vertically oriented and graded quasi-2D perovskites for efficient solar cells. *Adv Funct Mater* 2021;31:2008404. DOI
28. Li D, Xing Z, Huang L, et al. Spontaneous formation of upper gradient 2D structure for efficient and stable quasi-2D perovskites. *Adv Mater* 2021;33:e2101823. DOI PubMed

29. Zhou X, Wang Y, Li C, Wu T. Doping amino-functionalized ionic liquid in perovskite crystal for enhancing performances of hole-conductor free solar cells with carbon electrode. *Chem Eng J* 2019;372:46-52. DOI

30. Zhao H, Han Y, Xu Z, et al. A Novel anion doping for stable $CsPbI_2Br$ perovskite solar cells with an efficiency of 15.56% and an open circuit voltage of 1.30 V. *Adv Energy Mater* 2019;9:1902279. DOI

31. Shao M, Bie T, Yang L, et al. Over 21% efficiency stable 2D perovskite solar cells. *Adv Mater* 2022;34:e2107211. DOI PubMed

32. Zhu X, Du M, Feng J, et al. High-efficiency perovskite solar cells with imidazolium-based ionic liquid for surface passivation and charge transport. *Angew Chem Int Ed* 2021;60:4238-44. DOI PubMed

33. Liang J, Zhao P, Wang C, et al. $CsPb_{0.9}Sn_{0.1}IBr_2$ based all-inorganic perovskite solar cells with exceptional efficiency and stability. *J Am Chem Soc* 2017;139:14009-12. DOI

34. Thiesbrummel J, Le Corre VM, Peña-camargo F, et al. Universal current losses in perovskite solar cells due to mobile ions. *Adv Energy Mater* 2021;11:2101447. DOI

35. Shi J, Gao Y, Gao X, et al. Fluorinated low-dimensional ruddlesden-popper perovskite solar cells with over 17% power conversion efficiency and improved stability. *Adv Mater* 2019;31:e1901673. DOI PubMed